

Article

# Effects of Asymmetric Coupling Strength on Nonlinear Dynamics of Two Mutually Long-Delay-Coupled Semiconductor Lasers

Bin-Kai Liao <sup>1</sup>, Chin-Hao Tseng <sup>1</sup>, Yu-Chen Chu <sup>1</sup> and Sheng-Kwang Hwang <sup>1,2,\*</sup>

<sup>1</sup> Department of Photonics, National Cheng Kung University, Tainan 701, Taiwan; k95461634@gmail.com (B.-K.L.); l78081509@ncku.edu.tw (C.-H.T.); justin11323@gmail.com (Y.-C.C.)

<sup>2</sup> Advanced Optoelectronic Technology Center, National Cheng Kung University, Tainan 701, Taiwan

\* Correspondence: skhwang@mail.ncku.edu.tw

**Abstract:** This study investigates the effects of asymmetric coupling strength on nonlinear dynamics of two mutually long-delay-coupled semiconductor lasers through both experimental and numerical efforts. Dynamical maps and spectral features of dynamical states are analyzed as a function of the coupling strength and detuning frequency for a fixed coupling delay time. Symmetry in the coupling strength of the two lasers, in general, symmetrizes their dynamical behaviors and the corresponding spectral features. Slight to moderate asymmetry in the coupling strength moderately changes their dynamical behaviors from the ones when the coupling strength is symmetric, but does not break the symmetry of their dynamical behaviors and the corresponding spectral features. High asymmetry in the coupling strength not only strongly changes their dynamical behaviors from the ones when the coupling strength is symmetric, but also breaks the symmetry of their dynamical behaviors and the corresponding spectral features. Evolution of the dynamical behaviors from symmetry to asymmetry between the two lasers is identified. Experimental observations and numerical predictions agree not only qualitatively to a high extent but also quantitatively to a moderate extent.



**Citation:** Liao, B.-K.; Tseng, C.-H.; Chu, Y.-C.; Hwang, S.-K. Effects of Asymmetric Coupling Strength on Nonlinear Dynamics of Two Mutually Long-Delay-Coupled Semiconductor Lasers. *Photonics* **2022**, *9*, 28. <https://doi.org/10.3390/photonics9010028>

Received: 30 November 2021

Accepted: 31 December 2021

Published: 3 January 2022

**Publisher's Note:** MDPI stays neutral with regard to jurisdictional claims in published maps and institutional affiliations.



**Copyright:** © 2022 by the authors. Licensee MDPI, Basel, Switzerland. This article is an open access article distributed under the terms and conditions of the Creative Commons Attribution (CC BY) license (<https://creativecommons.org/licenses/by/4.0/>).

**Keywords:** semiconductor lasers; nonlinear dynamics; mutual coupling; asymmetric coupling strength; symmetry breaking

## 1. Introduction

Nonlinear dynamics of two mutually delay-coupled semiconductor lasers has attracted much research interest due to its profound physics and promising applications. By simply adjusting the operating conditions of the two lasers, including bias current, coupling strength, and detuning frequency, various dynamical behaviors can be induced, such as mutual injection locking, period-one (P1) dynamics, period-two (P2) dynamics, quasi-periodic dynamics, and chaos. The unique temporal and spectral features found in these dynamical behaviors have been proposed, respectively, to improve performance characteristics of existing technologies, such as enhancing the bandwidth of direct modulation [1–5] and suppressing nonlinear distortion due to direct modulation [6–8], or to provide alternatives for novel applications, such as tunable microwave generation [9–12], chaotic synchronization [13–16], reservoir computing [17–19], and decision making [20]. For these technological applications, the bias currents of the two lasers are, in general, adjusted independently and differently so that specific characteristics or functionalities are achieved. This inevitably leads to a difference in the coupling strength between the two lasers, i.e., the coupling strength is asymmetric.

Prior studies [21–25] that investigate nonlinear dynamical behaviors and their features in mutually coupled lasers mainly considered symmetric coupling strength only. The dynamical behaviors of the two lasers are mainly identical, i.e., symmetric, even though

symmetry breaking in their behaviors does happen over a limited range of operating condition. An interesting yet fundamental question to ask is whether the dynamical behaviors of the two lasers with asymmetric coupling strength are kept symmetric. For example, the result of a recent study [26], of which purpose focuses on showing that coupling strength asymmetry makes the mutually coupled laser system behave like a unidirectionally coupled laser system, indicates that their dynamical behaviors are still identical even when their coupling strength becomes slightly or moderately asymmetric. Would the dynamical behavior symmetry still hold if the extent of the coupling strength asymmetry enhances? The answer to this question is important not only for fundamental understandings about how and to what extent such a laser system responds to asymmetric coupling strength, but also for technological applications where such a laser system is expected to operate at a specific dynamical behavior all the time even when the coupling strength becomes asymmetric. However, this issue has not been much emphasized yet, and is thus numerically and experimentally investigated in this study using two mutually coupled lasers with a delay time longer than the relaxation resonance period of the lasers at free running. As shown in the following analyses, slight to moderate asymmetry in the coupling strength does not break the symmetry between the dynamical behaviors of the two lasers. Symmetry breaking of the dynamical behaviors happens when the coupling strength is highly asymmetric. Evolution of the dynamical behaviors from symmetry to asymmetry between the two lasers is observed, where numerical predictions and experimental observations agree not only qualitatively to a high extent but also quantitatively to a moderate extent.

The remainder of this paper is outlined as follows. In Section 2, the numerical model for two mutually delay-coupled semiconductor lasers, which is derived from the well-known Lang–Kobayashi equations, used in this study is described, and numerical predictions are demonstrated. In Section 3, the experimental setup of the laser system used in this study is introduced, and experimental observations are presented and compared with the numerical predictions shown in Section 2. Finally, a summary is given in Section 4.

## 2. Numerical Prediction

The dynamical behaviors of two mutually delay-coupled semiconductor lasers are numerically investigated in this section to obtain a picture of when, how, and to what extent changes in their dynamical behaviors happen if their coupling strength varies from symmetry to asymmetry. The numerical results would serve as a proper guidance for an experiment study demonstrated in Section 3 to verify the numerical predictions. Optical and microwave spectra presented here are obtained by considering the spontaneous emission noise of both lasers in the numerical calculation so that a fair comparison can be made with those obtained in the experimental study. Temporal evolutions shown here are calculated without taking into account the spontaneous emission noise of both lasers so that an easy comparison can be made between the outputs of the two lasers.

### 2.1. Numerical Model

Two mutually delay-coupled semiconductor lasers under study can be mathematically described by the following Lang–Kobayashi equations [27–30]:

Laser Diode 1 (LD1):

$$\frac{dA_1}{dt} = -\frac{\gamma_{c1}}{2} A_1 + i(\omega_{01} - \omega_{c1})A_1 + \frac{\Gamma_1}{2} g_1(1 - ib_1)A_1 + \eta_{21} A_2(t - \tau_2) e^{i\omega_{02}\tau_2} - i\Omega A_1 + F_{sp1} \tag{1}$$

$$\frac{dN_1}{dt} = \frac{J_1}{ed_1} - \gamma_{s1} N_1 - g_1 S_1. \tag{2}$$

Laser Diode 2 (LD2):

$$\frac{dA_2}{dt} = -\frac{\gamma_{c2}}{2}A_2 + i(\omega_{02} - \omega_{c2})A_2 + \frac{\Gamma_2}{2}g_2(1 - ib_2)A_2 + \eta_{12}A_1(t - \tau_1)e^{i\omega_{02}\tau_1} + F_{sp2} \quad (3)$$

$$\frac{dN_2}{dt} = \frac{J_2}{ed_2} - \gamma_{s2}N_2 - g_2S_2. \quad (4)$$

Here,  $A_j$  is the total complex intracavity field amplitude of LD $_j$ , where  $j = 1$  or  $2$ ,  $\gamma_{cj}$  is the cavity decay rate,  $\omega_{0j}$  is the free-running oscillation frequency,  $\omega_{cj}$  is the angular frequency of the cold cavity,  $\Gamma_j$  is the confinement factor describing the spatial overlap between the gain medium and the optical mode,  $b_j$  is the linewidth enhancement factor relating the dependence of the refractive index on changes in the optical gain,  $g_j$  is the optical gain parameter which is a function of the charge carrier density  $N_j$  and the intracavity photon density  $S_j$ ,  $F_{spj} = F_{rj} + iF_{ij}$  is the complex field noise,  $\eta_{12}$  and  $\eta_{21}$  are the injection coupling rates from LD1 to LD2 and from LD2 to LD1, respectively,  $\tau_1$  and  $\tau_2$  are the coupling delay times from LD1 to LD2 and from LD2 to LD1, respectively,  $f_i = \Omega/2\pi = (\omega_{01} - \omega_{02})/2\pi$  is the detuning frequency between LD1 and LD2 at free running,  $J_j$  is the bias current density,  $e$  is the electron charge,  $d_j$  is the active layer thickness, and  $\gamma_{sj}$  is the spontaneous carrier decay rate. The photon density is related to the intracavity field by:

$$S_j = \frac{2\epsilon_0 n_j^2}{\hbar\omega_{0j}} |A_j|^2 \quad (5)$$

where  $\epsilon_0$  is the free-space permittivity,  $n_j$  is the refractive index, and  $\hbar$  is the reduced Plank's constant. The gain coefficient  $g_j$  is a function of the photon density and carrier density described as:

$$g_j = \frac{\gamma_{cj}}{\Gamma_j} + \gamma_{nj} \frac{N_j - N_{0j}}{S_{0j}} - \gamma_{pj} \frac{S_j - S_{0j}}{\Gamma_j S_{0j}} \quad (6)$$

where  $\gamma_{nj}$  represents the differential carrier relaxation rate,  $\gamma_{pj}$  describes the nonlinear carrier relaxation rate,  $N_{0j}$  indicates the free-running carrier density, and  $S_{0j}$  expresses the free-running photon density, respectively.

For the purpose of numerical calculation, Equations (1)–(4) are recast about the steady-state, free-running operating point of each laser, where  $A_j = |A_{0j}|(a_{rj} + ia_{ij})$  and  $N_j = N_{0j}(1 + \tilde{n}_j)$  are used, and  $A_{0j}$  is the free-running field amplitude.

Laser Diode 1 (LD1):

$$\frac{da_{r1}}{dt} = \frac{1}{2} \left[ \frac{\gamma_{c1}\gamma_{n1}}{\gamma_{s1}\tilde{f}_1} \tilde{n}_1 - \gamma_{p1}(a_{r1}^2 + a_{i1}^2 - 1) \right] (a_{r1} + b_1 a_{i1}) + \Omega a_{i1} + \xi_{21}^s \gamma_{c1} [a_{r2}(t - \tau_2) \cos \omega_{02} \tau_2 - a_{i2}(t - \tau_2) \sin \omega_{02} \tau_2] + F_{a,r1} \quad (7)$$

$$\frac{da_{i1}}{dt} = \frac{1}{2} \left[ \frac{\gamma_{c1}\gamma_{n1}}{\gamma_{s1}\tilde{f}_1} \tilde{n}_1 - \gamma_{p1}(a_{r1}^2 + a_{i1}^2 - 1) \right] (-b_1 a_{r1} + a_{i1}) - \Omega a_{r1} + \xi_{21}^s \gamma_{c1} [a_{i2}(t - \tau_2) \cos \omega_{02} \tau_2 + a_{r2}(t - \tau_2) \sin \omega_{02} \tau_2] + F_{a,i1} \quad (8)$$

$$\frac{d\tilde{n}_1}{dt} = - \left[ \gamma_{s1} + \gamma_{n1}(a_{r1}^2 + a_{i1}^2) \right] \tilde{n}_1 - \gamma_{s1} \tilde{f}_1 (a_{r1}^2 + a_{i1}^2 - 1) + \frac{\gamma_{s1}\gamma_{p1}}{\gamma_{c1}} \tilde{f}_1 (a_{r1}^2 + a_{i1}^2) (a_{r1}^2 + a_{i1}^2 - 1). \quad (9)$$

Laser Diode 2 (LD2):

$$\frac{da_{r2}}{dt} = \frac{1}{2} \left[ \frac{\gamma_{c2}\gamma_{n2}}{\gamma_{s2}\tilde{J}_2} \tilde{n}_2 - \gamma_{p2}(a_{r2}^2 + a_{i2}^2 - 1) \right] (a_{r2} + b_2 a_{i2}) \quad (10)$$

$$\frac{da_{i2}}{dt} = \frac{1}{2} \left[ \frac{\gamma_{c2}\gamma_{n2}}{\gamma_{s2}\tilde{J}_2} \tilde{n}_2 - \gamma_{p2}(a_{r2}^2 + a_{i2}^2 - 1) \right] (-b_2 a_{r2} + a_{i2}) \quad (11)$$

$$\frac{d\tilde{n}_2}{dt} = - \left[ \gamma_{s2} + \gamma_{n2}(a_{r2}^2 + a_{i2}^2) \right] \tilde{n}_2 - \gamma_{s2}\tilde{J}_2(a_{r2}^2 + a_{i2}^2 - 1) + \frac{\gamma_{s2}\gamma_{p2}}{\gamma_{c2}} \tilde{J}_2(a_{r2}^2 + a_{i2}^2)(a_{r2}^2 + a_{i2}^2 - 1).$$

Here  $\xi_{12}^s = \eta_{12}|A_{01}|/\gamma_{c2}|A_{02}|$  and  $\xi_{21}^s = \eta_{21}|A_{02}|/\gamma_{c1}|A_{01}|$  represent the strength of coupling from LD1 to LD2 and from LD2 to LD1, respectively. A superscript s is used for both symbols to distinguish the coupling strength defined here from the one defined in the experimental study presented in Section 3. The normalized bias level is described by  $\tilde{J}_j = (J_j/ed_j - \gamma_{sj}N_j)/\gamma_{sj}N_j$ . The phase factor  $\omega_{02}\tau_j$  is set to zero throughout the numerical calculation in order to simplify the study. The normalized Langevin noise-source parameters  $F_{a_{rj}} = F_{rj}/|A_{0j}|$  and  $F_{a_{ij}} = F_{ij}/|A_{0j}|$  describe the real and imaginary parts of the normalized spontaneous emission parameters, respectively, and are characterized by a spontaneous emission rate as [31]:

$$\langle F_{a_{rj}}(t)F_{a_{rj}}(t') \rangle = \langle F_{a_{ij}}(t)F_{a_{ij}}(t') \rangle = \frac{R_{spj}}{2|A_{0j}|^2} \delta(t - t') \quad (13)$$

$$\langle F_{a_{rj}}(t)F_{a_{ij}}(t') \rangle = \langle F_{a_{ij}}(t)F_{a_{rj}}(t') \rangle = 0 \quad (14)$$

where  $R_{spj}$  represents the fraction of the spontaneous emission noise into the laser mode.

The values of the intrinsic laser parameters used for the numerical calculation here, which are experimentally measured using the four-wave mixing method [32], are shown in Table 1. Throughout the numerical calculation, the intrinsic laser parameters of LD1 and LD2 are set identical in order to simplify the study. Under this condition, the relaxation resonance frequency of either free-running laser is 10.25 GHz. A second-order Runge–Kutta method with the measured laser parameters is used to solve Equations (7)–(12). Throughout the numerical study, a time duration of about 0.47 ps is used for one integration step, and a time duration of 1  $\mu$ s is adopted for complete integration.

**Table 1.** The values of laser parameters used in the numerical calculation.

| Parameter                            | Symbol                     | Value   |
|--------------------------------------|----------------------------|---|
| Linewidth enhancement factor         | $b_1, b_2$                 | 3   |
| Normalized bias level                | $\tilde{J}_1, \tilde{J}_2$ | 1.222   |
| Coupling delay time                  | $\tau_1, \tau_2$           | 40.15 ns  |
| Cavity decay rate                    | $\gamma_{c1}, \gamma_{c2}$ | $5.36 \times 10^{11} \text{ s}^{-1}$                            |
| Spontaneous carrier relaxation rate  | $\gamma_{s1}, \gamma_{s2}$ | $5.96 \times 10^9 \text{ s}^{-1}$                               |
| Differential carrier relaxation rate | $\gamma_{n1}, \gamma_{n2}$ | $7.53 \times 10^9 \text{ s}^{-1}$                               |
| Nonlinear carrier relaxation rate    | $\gamma_{p1}, \gamma_{p2}$ | $1.91 \times 10^{11} \text{ s}^{-1}$                            |
| Spontaneous emission rate            | $R_{sp1}, R_{sp2}$         | $4.7 \times 10^{18} \text{ V}^2\text{m}^{-1}\text{s}^{-1}$ [31] |

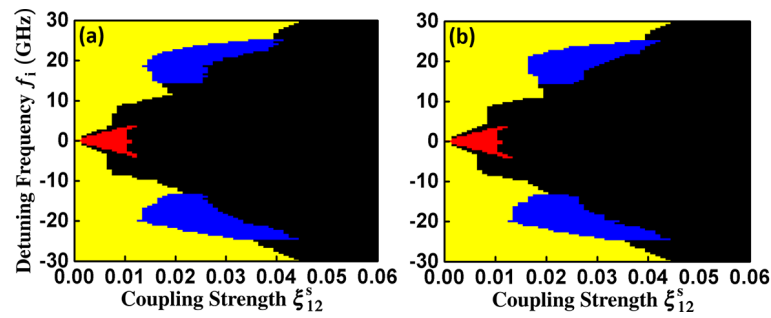
### 2.2. Dynamics Behaviors under Symmetric Coupling Strength

For the purpose of comparison, the dynamical behavior of the mutually delay-coupled laser system is first investigated when the coupling strength is symmetric, i.e.,  $\xi_{12}^s = \xi_{21}^s$ , in this subsection. To obtain a global understanding of how the laser system behaves at a fixed coupling delay time of 40.15 ns under study, maps of dynamical states as a function of

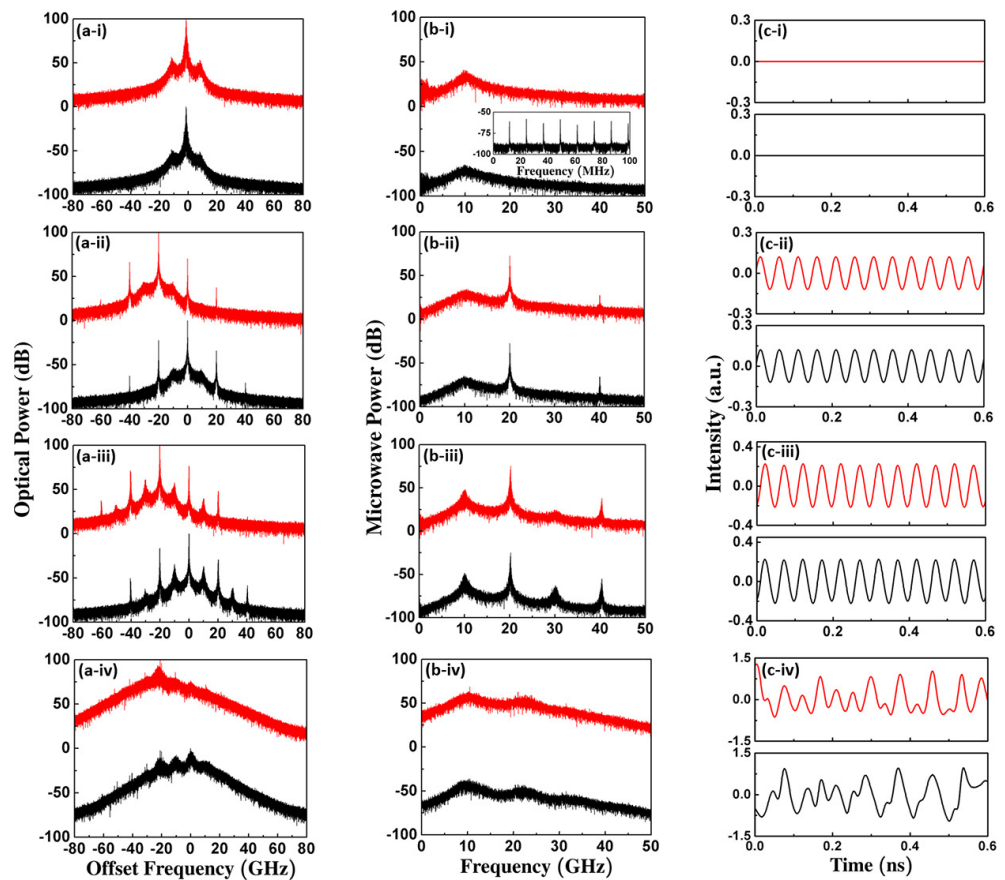
$\zeta_{12}^s$  and  $f_i$  for LD1 and LD2 are presented in Figure 1a and Figure 1b, respectively. Regions of mutual injection locking, P1 dynamics, P2 dynamics, and chaos are marked by red, yellow, blue, and black, respectively. Periodic dynamics with periods higher than two are included in the regions of chaos. Comparing Figure 1a with Figure 1b demonstrates that the dynamical behaviors of both lasers are generally identical over the range of  $\zeta_{12}^s$  and  $f_i$  under study when the coupling strength is symmetric. In addition, each different dynamical state generally appears symmetrically with respect to  $f_i = 0$ . The mutual injection locking states emerge at weak coupling strength and small frequency detuning. The P1 dynamical states appear when  $\zeta_{12}^s$  is smaller than 0.044 over the range of  $f_i$  under study. The chaotic states start to emerge when  $\zeta_{12}^s$  is greater than 0.007. Note that the coupling delay time, 40.15 ns, is chosen here according to the one used in the experimental setup described in Section 3 so that fair comparisons can be made between numerical and experimental results demonstrated in Section 3.

Figure 2 shows the typical optical spectrum, microwave spectrum, and temporal evolution for each different dynamical state of LD1 (red curve) and LD2 (black curve) presented in Figure 1. Note that the frequency axes of all the optical spectra shown in this study are relative to the free-running oscillation frequency of LD2. As Figure 2(a-i) shows, where  $(\zeta_{12}^s, f_i) = (0.009, -2.9 \text{ GHz})$ , both LD1 and LD2 oscillate at the same offset frequency of  $-1.52 \text{ GHz}$ , indicating that mutual injection locking is established between the two lasers. Two relaxation resonance sidebands appear 10 GHz away from the principal oscillation with the lower one being slightly stronger due to the positive value of  $b$ . As Figure 2(b-i) presents, photodetection of the optical signal generates a spectral component at 10 GHz due to the relaxation resonance and a small bump around 0 GHz. The bump actually consists of several spectral components that are equally separated by 12.45 MHz, as the inset shows. The frequency separation corresponds to the loop frequency of the round-trip delay coupling between the two lasers, i.e., the reciprocal of the summation of the two coupling delay times. The appearance of such loop modes is a typical feature of a delay-coupled system because an additional resonance condition given by the round-trip delay coupling is required for the system to satisfy. As Figure 2(c-i) shows, the intensity of both lasers is constant over time yet with an extremely weak modulation at the loop frequency, 12.45 MHz, which can be hardly observed with bare eyes. Note that the intensity value shown in the figures of this section is calculated by removing the direct-current component of each signal. As Figure 2(c-i) also presents, the temporal evolution of the intensity is identical between the two lasers. In fact, LD1 leads LD2 by about 40.15 ns (i.e., the coupling delay time) in Figure 2(c-i) where the temporal evolution of the LD1 intensity is shifted by about 40.15 ns for easy comparison.

As Figure 2(a-ii) shows, where  $(\zeta_{12}^s, f_i) = (0.011, -20 \text{ GHz})$ , either LD1 or LD2 oscillates at a frequency that is slightly red-shifted from its free-running oscillation frequency due to the injection pushing effect [33]. Moreover, oscillation sidebands appear around the principal oscillation of each laser, which are equally separated by an oscillation frequency of  $f_0 = 20.06 \text{ GHz}$ . Such a spectral feature is a typical signature of the P1 dynamics. This generates a microwave at  $f_0 = 20.06 \text{ GHz}$  and its harmonics after photodetection, as illustrated in Figure 2(b-ii), which is highly advantageous for high-frequency microwave generation [34–38]. Due to the round-trip delay coupling, there also appears a small bump around 0 GHz, which consists of several spectral components equally separated by 12.45 MHz, as those shown in the inset of Figure 2(b-i). Similar closely-spaced spectral components also appear on top of each P1 spectral component shown in Figure 2(b-ii). As Figure 2(c-ii) shows, the intensity of either laser oscillates sinusoidally with a single period equal to the reciprocal of  $f_0 = 20.06 \text{ GHz}$ . The sinusoidal intensity oscillation of either laser is, in fact, extremely weakly modulated at the loop frequency, 12.45 MHz, which can be hardly observed with bare eyes. As Figure 2(c-ii) also presents, the temporal evolution of the intensity oscillation is identical between the two lasers yet with LD1 leading LD2 by about 40.15 ns, corresponding to the coupling delay time. For easy comparison, the temporal evolution of the LD1 intensity is shifted by about 40.15 ns in Figure 2(c-ii).



**Figure 1.** Maps of dynamical states for (a) LD1 and (b) LD2, respectively, in the mutually-coupled laser system when  $\xi_{12}^s = \xi_{21}^s$ . Regions of mutual injection locking, P1 dynamics, P2 dynamics, and chaos are marked by red, yellow, blue, and black, respectively.



**Figure 2.** (a) Optical spectra, (b) microwave spectra, and (c) temporal evolutions of LD1 (red curve) and LD2 (black curve) for (i) mutual injection locking at  $(\xi_{12}^s, f_i) = (0.009, -2.9 \text{ GHz})$ , (ii) P1 dynamics at  $(\xi_{12}^s, f_i) = (0.011, -20 \text{ GHz})$ , (iii) P2 dynamics at  $(\xi_{12}^s, f_i) = (0.02, -20 \text{ GHz})$ , and (iv) chaos at  $(\xi_{12}^s, f_i) = (0.05, -20 \text{ GHz})$ . The inset of (b-i) shows the enlargement of the microwave spectrum for LD2 around 0 GHz. The  $x$ -axes in (a) are relative to the free-running oscillation frequency of LD2. The red curves in (a,b) are up-shifted by 100 dB for clear visibility.

By increasing the coupling strength so that  $(\xi_{12}^s, f_i) = (0.02, -20 \text{ GHz})$ , as Figure 2(a-iii) shows, while the spectral components observed in Figure 2(a-ii) for either laser are similarly kept with a slight increase in their frequency separation, leading to  $f_0 = 20.21 \text{ GHz}$ , subharmonics emerge in the midway between the spectral components. Such a spectral feature is a typical signature of the P2 dynamics. The beating between the spectral components at the photodetector not only gives rise to a microwave at  $f_0 = 20.21 \text{ GHz}$  and its harmonics, but also leads to subharmonics at the midway between the spectral components,

as Figure 2(b-iii) shows. Due to the round-trip delay coupling, there also appears a small bump around 0 GHz, which consists of several spectral components equally separated by 12.45 MHz, as those shown in the inset of Figure 2(b-i). Similar closely-spaced spectral components also appear on top of each P2 spectral component shown in Figure 2(b-iii). As Figure 2(c-iii) shows, not only does the intensity of either laser oscillate sinusoidally with a period equal to the reciprocal of  $f_0 = 20.21$  GHz, but the intensity oscillation is also moderately modulated with a period equal to two times the reciprocal of  $f_0 = 20.21$  GHz. Such a moderately modulated intensity oscillation is also extremely weakly modulated at the loop frequency, 12.45 MHz, which can be hardly observed with bare eyes. As Figure 2(c-iii) also presents, the temporal evolution of the moderately modulated intensity oscillation is almost identical between the two lasers. In fact, LD1 leads LD2 by about 40.15 ns (i.e., the coupling delay time) in Figure 2(c-iii) where the temporal evolution of the LD1 intensity is shifted by about 40.15 ns for easy comparison.

By continuing to increase the coupling strength so that  $(\zeta_{12}^s, f_i) = (0.05, -20 \text{ GHz})$ , as Figure 2(a-iv) shows, a broad and continuous spectral distribution appears for either laser, which is a typical signature of chaos. After photodetection, as Figure 2(b-iv) presents, such a spectral feature generates a broadband chaotic microwave with a spectral distribution of more than 40 GHz, which is highly advantageous for chaos-based applications, such as high-resolution chaotic radars [39–42], high-speed chaotic communication [43–46], and high-entropy random number generation [47–50]. Owing to the round-trip delay coupling, spectral components that are equally separated by 12.45 MHz, as those shown in the inset of Figure 2(b-i) yet with much weaker intensity, also emerge on top of the spectral distribution in Figure 2(b-iv). As Figure 2(c-iv) shows, the intensity of both lasers oscillates irregularly, and is extremely weakly modulated at the loop frequency, 12.45 MHz, which can be hardly be observed with bare eyes. The temporal evolution of the intensity oscillation is similar between the two lasers with LD1 leading LD2 by about 40.15 ns, corresponding to the coupling delay time. For easy comparison, the temporal evolution of the LD1 intensity is shifted by about 40.15 ns in Figure 2(c-iv).

As observed from Figure 2(a-ii) to Figure 2(a-iv), the laser system follows a period-doubling route to chaos as  $\zeta_{12}^s$  increases at  $f_i = -20$  GHz. A similar route is also found when  $f_i$  falls between  $-24$  GHz and  $-13$  GHz and between 15 GHz and 26 GHz, as Figure 1 presents. The results obtained in either Figure 1 or Figure 2 conclude that the dynamical behaviors of both lasers are, in general, symmetric when the coupling strength is symmetric, which agrees with the observations in prior studies [23–25].

### 2.3. Dynamics Behaviors under Asymmetric Coupling Strength

In the following analyses, to investigate how the two lasers react when the coupling strength becomes asymmetric, the strength of the coupling from LD2 to LD1 is fixed at  $\zeta_{21}^s = 0.01$  and 0.001, respectively, while the strength of the coupling from LD1 to LD2 is varied from  $\zeta_{12}^s = 0$  to 0.06. As noted, while  $\zeta_{21}^s = 0.01$  is about the same order of magnitude as  $\zeta_{12}^s$ ,  $\zeta_{21}^s = 0.001$  is about an order of magnitude smaller than  $\zeta_{12}^s$ . Maps of dynamical states as a function of  $\zeta_{12}^s$  and  $f_i$  for LD1 and LD2 when  $\zeta_{21}^s = 0.01$  are presented in Figure 3(a-i) and Figure 3(b-i), respectively, at a fixed coupling delay time of 40.15 ns. Note that periodic dynamics with periods higher than two are included in the regions of chaos. Comparing Figure 3(a-i,b-i) with Figure 1 shows that, while the regions of chaos suppress moderately, the regions of mutual injection locking and P1 dynamics expand moderately. The spectral features of different nonlinear dynamical states in Figure 3(a-i,b-i) are closely similar to those presented in Figure 2. Comparing Figure 3(a-i) with Figure 3(b-i) demonstrates that the dynamical behaviors of the two lasers are generally symmetric at the extent of the coupling strength asymmetry under study here.

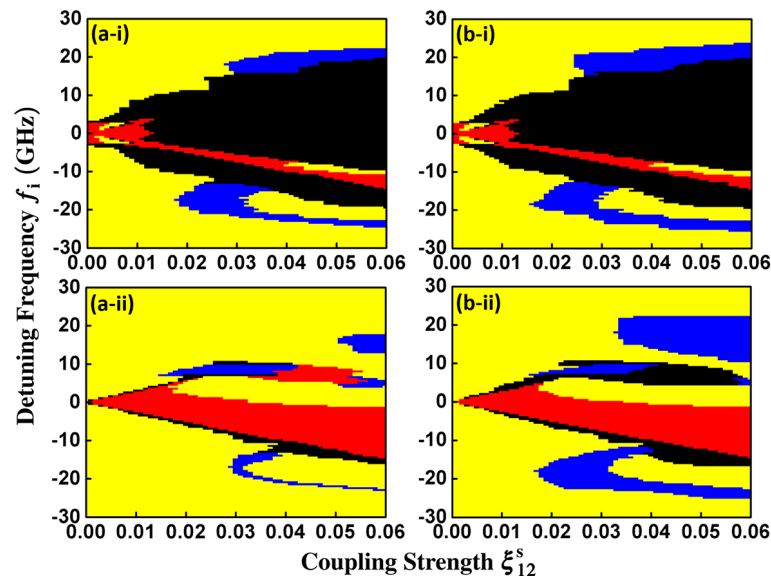


**Figure 3.** Maps of dynamical states for (a) LD1 and (b) LD2, respectively, in the mutually coupled laser system when (i)  $\zeta_{21}^s = 0.01$  and (ii)  $\zeta_{21}^s = 0.001$ . Regions of mutual injection locking, P1 dynamics, P2 dynamics, and chaos are marked by red, yellow, blue, and black, respectively.

Such dynamical behavior symmetry is, however, not guaranteed if the extent of the coupling strength asymmetry increases, as Figure 3(a-ii,b-ii) demonstrate, where  $\zeta_{21}^s$  is reduced from 0.01 to 0.001. While the dynamical behaviors of the two lasers are symmetric over most of the operating conditions considered here, asymmetry happens over a region where  $\zeta_{12}^s$  falls between 0.034 and 0.06 and  $f_i$  is between 11 GHz and 22 GHz, a region where  $\zeta_{12}^s$  falls between 0.03 and 0.055 and  $f_i$  is between 7 GHz and 10 GHz, and a region where  $\zeta_{12}^s$  falls between 0.018 and 0.06 and  $f_i$  is between  $-25$  GHz and  $-12$  GHz. Comparing Figure 3(a-ii,b-ii) with Figure 3(a-i,b-i) shows that, as  $\zeta_{21}^s$  is reduced, the regions of mutual injection locking and P1 dynamics continue to expand and thus become dominant, while the regions of chaos continues to suppress.

To investigate how the dynamical behaviors of both lasers evolve from symmetry to asymmetry when  $\zeta_{21}^s = 0.001$ , a development of optical spectra, microwave spectra, and temporal evolutions for LD1 (red curve) and LD2 (black curve) is presented in Figure 4 when  $\zeta_{12}^s$  is adjusted and  $f_i$  is fixed at 9 GHz. At  $\zeta_{12}^s = 0.0019$ , either LD1 or LD2 behaves as a P1 dynamical state with an oscillation frequency of about 9 GHz, as either Figure 4(a-i), Figure 4(b-i), or Figure 4(c-i) presents. The temporal evolution of the intensity oscillation is identical between the two lasers yet with LD1 lagging LD2 by about 40.15 ns, as Figure 4(c-i) shows where the temporal evolution of the LD2 intensity is shifted by about 40.15 ns.

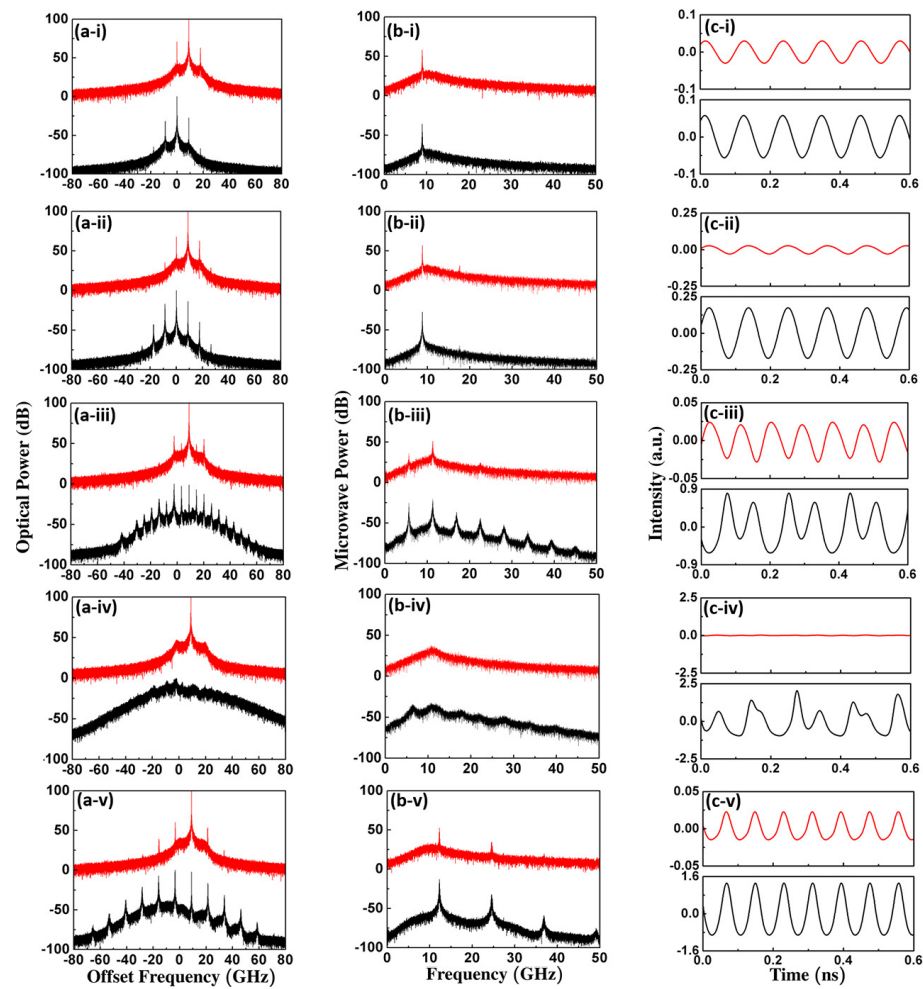


**Figure 4.** (a) Optical spectra, (b) microwave spectra, and (c) temporal evolutions of LD1 (red curve) and LD2 (black curve) for (i)  $\zeta_{12}^s = 0.0019$ , (ii)  $\zeta_{12}^s = 0.006$ , (iii)  $\zeta_{12}^s = 0.028$ , (iv)  $\zeta_{12}^s = 0.048$ , and (v)  $\zeta_{12}^s = 0.055$ , respectively, when  $\zeta_{21}^s = 0.001$  and  $f_i = 9$  GHz. The x-axes in (a) are relative to the free-running oscillation frequency of LD2. The red curves in (a,b) are up-shifted by 100 dB for clear visibility.

As  $\zeta_{12}^s$  is increased to 0.006, either LD1 or LD2 still behaves as a P1 dynamical state yet with an oscillation frequency of about 8.87 GHz, as either Figure 4(a-ii), Figure 4(b-ii), or Figure 4(c-ii) presents. The temporal evolution of the intensity oscillation is identical between the two lasers yet with LD1 lagging LD2 by about 40.15 ns, as Figure 4(c-ii) presents where the temporal evolution of the LD2 intensity is shifted by about 40.15 ns. While the microwave spectral features and temporal evolutions between the two lasers look highly similar in Figure 4(b-ii) and Figure 4(c-ii), respectively, a slight deviation exists in their optical spectral features in Figure 4(a-ii). Not only a few more spectral components appear in LD2, but also the principal oscillation becomes less dominant, making the optical spectral profile of LD2 more widely distributed. This implies that the two lasers start to behave differently in a subtle manner even though they both behave as a P1 dynamical state. Such a deviation becomes more significant when  $\zeta_{12}^s$  is further increased to 0.028, as Figure 4(a-iii) shows. Both lasers now evolve into a P2 dynamical state, as more evidently observed in Figure 4(b-iii) where subharmonics emerge in the midway of spectral components at the integral multiples of 11.29 GHz, and also in Figure 4(c-iii) where an intensity oscillation with a period equal to the reciprocal of 11.29 GHz is moderately modulated with a period equal to two times the reciprocal of 11.29 GHz. As noted, the temporal evolution of the moderately modulated intensity oscillation becomes moderately dissimilar between the

two lasers with LD1 leading LD2 by about 40.15 ns, as Figure 4(c-iii) presents where the temporal evolution of the LD1 intensity is shifted by about 40.15 ns.

As  $\zeta_{12}^s$  continues to increase to 0.048, the optical spectra, microwave spectra, and temporal evolutions of both lasers shown in Figure 4(a-iv), Figure 4(b-iv), and Figure 4(c-iv), respectively, exhibit completely different features and profiles. On one hand, as Figure 4(a-iv) shows, LD1 oscillates at an offset frequency of 9 GHz that is surrounded by two low-intensity spectral components about 11 GHz away. The two low-intensity components result from the modified relaxation resonance of LD1 due to the optical injection from LD2. Such a modification leads to the enhancement of the relaxation resonance frequency, which is more clearly identified in Figure 4(b-iv) where the microwave spectrum peaks at around 11 GHz. This indicates that LD1 now emits a continuous-wave optical output with a slightly higher relaxation resonance frequency as compared with its free-running condition, which is verified by Figure 4(c-iv) where the LD1 intensity remains constant over time. On the other hand, as either Figure 4(a-iv) or Figure 4(b-iv) shows, a broad and continuous spectral distribution is observed for LD2, indicating that LD2 now behaves as a chaotic state, which is verified by Figure 4(c-iv) where the LD2 intensity oscillates irregularly.

By further increasing  $\zeta_{12}^s$  to 0.055, either LD1 or LD2 behaves as a P1 dynamical state with an oscillation frequency of about 12.28 GHz, as either Figure 4(a-v), Figure 4(b-v), or Figure 4(c-v) presents. While the microwave spectral features and temporal evolutions of both lasers look highly similar in Figure 4(b-v,c-v), a distinct deviation exists in their optical spectral features in Figure 4(a-v). Not only do a few more spectral components emerge in LD2, but the principal oscillation also becomes less dominant, making the optical spectral profile of LD2 more widely distributed. This implies that the two lasers behave differently in a subtle manner even though they both behave as a P1 dynamical state.

The extremest case for the dynamical behavior asymmetry happens when  $\zeta_{21}^s = 0$ . This indicates that no optical injection is introduced from LD2 to LD1 and the laser system therefore works as a unidirectional optical injection system. Under such an operating condition, the distribution of dynamical states as a function of  $\zeta_{12}^s$  and  $f_i$  for LD2 is greatly similar to the one presented in Figure 3(b-ii), while LD1 is kept at its free-running operation and thus emits a continuous-wave optical output no matter how  $\zeta_{12}^s$  and  $f_i$  are adjusted.

The results shown in Figures 1–4 indicate that the dynamical behavior of the laser system could change when the coupling strength becomes asymmetric. This suggests that if a specific dynamical behavior is used for applications where a difference in the coupling strength between the two lasers is likely to happen in order to achieve certain features or functionalities, care must be taken so that the laser system is operated at the same dynamical behavior even when the coupling strength becomes asymmetric during operation. In addition, the results also demonstrate that the dynamical behaviors of the two lasers could become asymmetric when the coupling strength becomes highly asymmetric. This suggests that if both lasers are expected to simultaneously operate at a specific dynamical behavior all the time for applications, care must be taken either to avoid the operation of the laser system with highly asymmetric coupling strength, or to avoid the operation of the laser system over regions where symmetry breaking in the dynamical behavior happens.

### 3. Experimental Observation

In the previous section, the dynamical behaviors of two mutually delay-coupled semiconductor lasers are numerically investigated when their coupling strength becomes asymmetric. Slight to moderate asymmetry in the coupling strength moderately changes their dynamical behaviors from the ones when the coupling strength is symmetric, but does not break the symmetry of their dynamical behaviors and spectral features. High asymmetry in the coupling strength, however, not only strongly changes their dynamical behaviors from the ones when the coupling strength is symmetric, but also breaks the symmetry of their dynamical behaviors and spectral features. In this section, an experimental study is carried out to verify the numerical predictions.

### 3.1. Experimental Setup

A schematic diagram of a mutually long-delay-coupled laser system consisting of two single-mode distributed feedback semiconductor lasers, LD1 (Furukawa FRL15DCW5-A81) and LD2 (Furukawa FRL15DCW5-A81), is presented in Figure 5a. The two lasers are mutually coupled by optical injection from one to the other through an optical circulator in each optical injection route, as the blue or red path indicates. For LD2, its bias current and temperature are fixed at 70 mA and 18.9 °C, respectively, throughout the study. This results in a free-running oscillation frequency of 193.28 THz, an output power of 15.48 mW, and a relaxation resonance frequency of 10 GHz. For LD1, while its bias current is fixed at 70 mA throughout the study, its temperature is slightly adjusted around 25.57 °C in order to detune its free-running oscillation frequency away from 193.28 THz (i.e., the free-running oscillation frequency of LD2) by  $f_i$  for the excitation of possible dynamical behaviors. The free-running LD1 therefore emits an output power varying slightly around 13.43 mW, depending on the temperature adjustment, with a relaxation resonance frequency of 10 GHz. A variable optical attenuator in each optical injection route adjusts the power of the optical injection (i.e., the coupling strength) from one laser to the other. For the experimental analysis, the coupling strength received by LD2,  $\zeta_{12}^e$ , is defined as the square root of the power ratio between the optical injection from LD1 and the free-running LD2. Similarly, the coupling strength received by LD1,  $\zeta_{21}^e$ , is defined as the square root of the power ratio between the optical injection from LD2 and the free-running LD1. Note that a superscript e is used for both symbols to distinguish the coupling strength defined here from the one defined in the numerical investigation presented in Section 2. These definitions differ by a factor of  $\eta_{12}/\gamma_{c2}$  for coupling from LD1 to LD2 and  $\eta_{21}/\gamma_{c1}$  for coupling from LD2 to LD1, respectively. According to the values of  $\eta_{12}$ ,  $\eta_{21}$ ,  $\gamma_{c1}$ , and  $\gamma_{c2}$  used in the simulation of this study, as previously indicated, the coupling strength defined in the experimental study is about an order of magnitude larger than that defined in the numerical investigation for a given ratio between the fields of the optical injection and the injected laser. Polarization maintaining fibers are used for all the optical devices and components to keep the polarization states of both lasers unchanged. Both optical injection routes have approximately the same fixed length, which corresponds to a coupling delay time of about 40.15 ns from one laser to the other. Such a delay time is longer than the relaxation resonance period of either laser used here. To investigate the spectral features of LD1 and LD2 outputs, respectively, one output port of each fiber coupler in Figure 5a is connected to a detection system consisting of an optical spectrum analyzer (Advantest Q8384) and a microwave spectrum analyzer (Keysight PXAN9030A) following a 50-GHz photodetector (u2t Photonics XPDV2120R), as shown in Figure 5b.

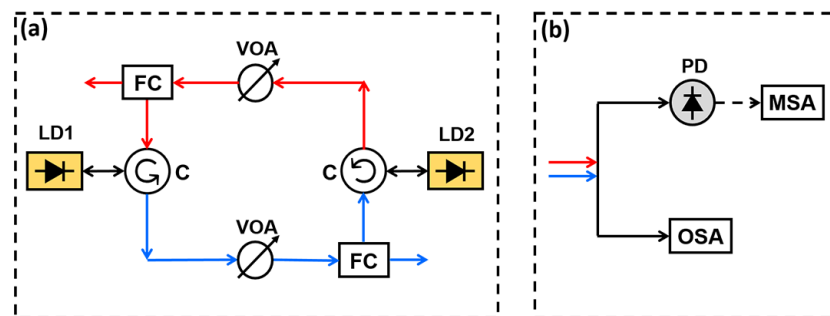


**Figure 5.** Schematic diagram of (a) a mutually delay-coupled laser system and (b) a detection system. LD1, laser diode 1; LD2, laser diode 2; FC, fiber coupler; C, circulator; VOA, variable optical attenuator; PD, photodetector; OSA, optical spectrum analyzer; and MSA, microwave spectrum analyzer.

### 3.2. Dynamical Behaviors under Symmetric Coupling Strength

The dynamical behavior of the mutually delay-coupled laser system is first studied when the coupling strength is symmetric, i.e.,  $\zeta_{12}^e = \zeta_{21}^e$ , in this subsection. To obtain a global understanding of how the laser system behaves at a fixed coupling delay time of

40.15 ns under consideration, maps of dynamical states as a function of  $\zeta_{12}^e$  and  $f_i$  for LD1 and LD2 are presented in Figure 6a and Figure 6b, respectively. Regions of mutual injection locking, P1 dynamics, P2 dynamics, and chaos are marked by red, yellow, blue, and black, respectively. Periodic dynamics with periods higher than two are included in the regions of chaos. Comparing Figure 6a with Figure 6b demonstrates that the dynamical behaviors of both lasers are generally identical over the range of  $\zeta_{12}^e$  and  $f_i$  under study when the coupling strength is symmetric. This experimental observation is consistent with the numerical prediction presented in Figure 1. Except for the P2 dynamical states that only appear over a small region where  $f_i$  falls between  $-26$  GHz and  $-14$  GHz, other nonlinear dynamical states generally appear symmetrically with respect to  $f_i = 0$ . The mutual injection locking states emerge at weak coupling strength and small frequency detuning. The P1 dynamical states appear when  $\zeta_{12}^e$  is smaller than 0.21 over the range of  $f_i$  under study. The chaotic states start to emerge when  $\zeta_{12}^e$  is greater than 0.1. Comparing Figure 6 with Figure 1 shows that, except for the P2 dynamical states that appear over a region where  $f_i$  falls between 15 GHz and 26 GHz only in the numerical result, the distribution of different dynamical states as a function of  $\zeta_{12}^e$  and  $f_i$  is highly similar. For example, the mutual injection locking states appear when  $\zeta_{12}^e$  is smaller than 0.125 in Figure 6 and when  $\zeta_{12}^s$  is smaller than 0.012 in Figure 1, while the chaotic states start to emerge when  $\zeta_{12}^e$  is greater than 0.1 in Figure 6 and when  $\zeta_{12}^s$  is greater than 0.007 in Figure 1. Considering that  $\zeta_{12}^e$  is by definition about an order of magnitude larger than  $\zeta_{12}^s$ , these results demonstrate that the numerical model used here reproduces the experimental observations not only qualitatively to a high extent but also quantitatively to a moderate extent.

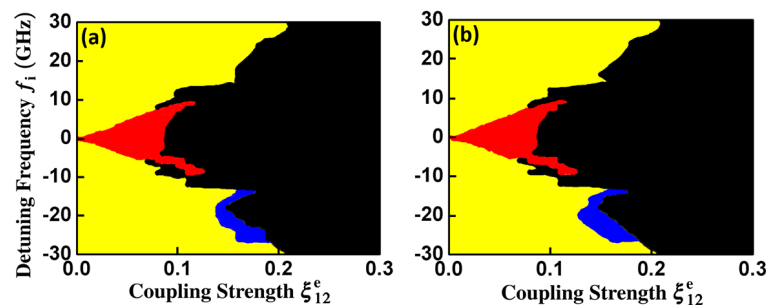


**Figure 6.** Maps of dynamical states for (a) LD1 and (b) LD2, respectively, in the mutually coupled laser system when  $\zeta_{12}^e = \zeta_{21}^e$ . Regions of mutual injection locking, P1 dynamics, P2 dynamics, and chaos are marked by red, yellow, blue, and black, respectively.

Figure 7 shows the typical optical and microwave spectra for each different dynamical state of LD1 (red curve) and LD2 (black curve) presented in Figure 6. Note that the frequency axes of all the optical spectra shown in this study are relative to the free-running oscillation frequency of LD2. As Figure 7(a-i) shows, where  $(\zeta_{12}^e, f_i) = (0.06, -5$  GHz), both LD1 and LD2 oscillate at the same offset frequency of  $-2.84$  GHz, indicating that mutual injection locking is established between the two lasers. Photodetection of such an optical signal only generates a small bump around 0 GHz, as Figure 7(b-i) presents. The bump actually consists of several spectral components that are equally separated by 12.45 MHz, as the inset shows, which corresponds to the loop frequency of the round-trip delay coupling between the two lasers. The loop modes are not observed in Figure 7(a-i) due to the limited resolution, about 0.01 nm at the wavelength of 1550 nm, of the optical spectrum analyzer used in this study.

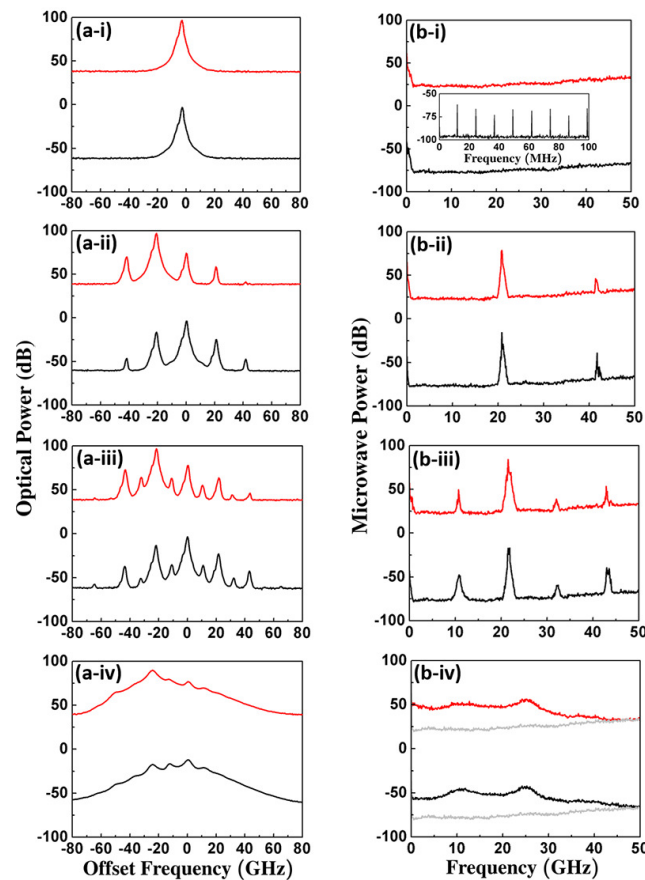


**Figure 7.** (a) Optical spectra and (b) microwave spectra of LD1 (red curve) and LD2 (black curve) for (i) mutual injection locking at  $(\zeta_{12}^e, f_i) = (0.06, -5 \text{ GHz})$ , (ii) P1 dynamics at  $(\zeta_{12}^e, f_i) = (0.1, -20 \text{ GHz})$ , (iii) P2 dynamics at  $(\zeta_{12}^e, f_i) = (0.15, -20 \text{ GHz})$ , and (iv) chaos at  $(\zeta_{12}^e, f_i) = (0.28, -20 \text{ GHz})$ . The inset of (b-i) shows the enlargement of the microwave spectrum for LD2 around 0 GHz. The x-axes in (a) are relative to the free-running oscillation frequency of LD2. The red curves in (a,b) are up-shifted by 100 dB for clear visibility. The gray curves in (b-iv) show the noise floor of the laser system.

As Figure 7(a-ii) shows, where  $(\zeta_{12}^e, f_i) = (0.1, -20 \text{ GHz})$ , either LD1 or LD2 oscillates at a frequency that is slightly red-shifted from its free-running oscillation frequency. In addition, oscillation sidebands emerge around the principal oscillation of each laser, which are equally separated by an oscillation frequency of  $f_0 = 20.8 \text{ GHz}$ . Such a spectral feature is a typical signature of the P1 dynamics. Photodetection of the optical signal generates a microwave at  $f_0 = 20.8 \text{ GHz}$  and its harmonics, as illustrated in Figure 7(b-ii). Due to the round-trip delay coupling, there also appears a small bump around 0 GHz, which consists of several spectral components equally separated by 12.45 MHz, as those shown in the inset of Figure 7(b-i). Similar closely-spaced spectral components also appear on top of each P1 spectral component shown in Figure 7(b-ii).

By increasing the coupling strength so that  $(\zeta_{12}^e, f_i) = (0.15, -20 \text{ GHz})$ , as Figure 7(a-iii) shows, while the spectral components observed in Figure 7(a-ii) for either laser are similarly kept with a slight increase in their frequency separation, leading to  $f_0 = 21.5 \text{ GHz}$ , subharmonics emerge in the midway between the spectral components. Such a spectral feature is a typical signature of the P2 dynamics. The beating between the spectral components at the photodetector not only gives rise to a microwave at  $f_0 = 21.5 \text{ GHz}$  and its harmonics, but also leads to subharmonics at the midway between the spectral components, as Figure 7(b-iii) shows. As observed, due to the round-trip delay coupling, there also appears a small bump around 0 GHz, which consists of several spectral components equally separated by 12.45 MHz, as those shown in the inset of Figure 7(b-i). Similar

closely-spaced spectral components also appear on top of each P2 spectral component shown in Figure 7(b-iii).

By continuing to increase the coupling strength so that  $(\zeta_{12}^e, f_i) = (0.28, -20 \text{ GHz})$ , as Figure 7(a-iv) shows, a broad and continuous spectral distribution appears for either laser, which is a typical signature of chaos. After photodetection, as Figure 7(b-iv) presents, such a spectral feature generates a broadband chaotic microwave with a spectral distribution of more than 40 GHz. Due to the round-trip delay coupling, spectral components that are equally separated by 12.45 MHz, as those shown in the inset of Figure 7(b-i) yet with much weaker intensity, also emerge on top of the spectral distribution in Figure 7(b-iv).

As noted from Figure 7(a-ii) to Figure 7(a-iv), the laser system follows a period-doubling route to chaos as  $\zeta_{12}^e$  increases at  $f_i = -20 \text{ GHz}$ , which agrees with the numerical prediction shown in Figure 2. A similar route is also found when  $f_i$  falls between  $-26 \text{ GHz}$  and  $-14 \text{ GHz}$ , as demonstrated in Figure 7. The observations found in either Figure 6 or Figure 7 conclude that the dynamical behaviors of both lasers are, in general, symmetric when the coupling strength is symmetric, which verifies the numerical predictions demonstrated in either Figure 1 or Figure 2.

### 3.3. Dynamics Behaviors under Asymmetric Coupling Strength

To study how the two lasers respond when the coupling strength becomes asymmetric, the strength of the coupling from LD2 to LD1 is fixed at  $\zeta_{21}^e = 0.01$ , while the strength of the coupling from LD1 to LD2 is varied from  $\zeta_{12}^e = 0$  to 0.3. Note that  $\zeta_{21}^e = 0.01$  is an order of magnitude smaller than  $\zeta_{12}^e$ , and is so chosen that the dynamical behavior asymmetry could happen based on the numerical prediction found in Section 2.3. Maps of dynamical states as a function of  $\zeta_{12}^e$  and  $f_i$  for LD1 and LD2 are presented in Figure 8a and Figure 8b, respectively, at a fixed coupling delay time of 40.15 ns. Note that periodic dynamics with periods higher than two are included in the regions of chaos. Comparing Figure 8 with Figure 6 shows that, while the regions of chaos shrink dramatically, the regions of mutual injection locking and P1 dynamics largely expand and become dominant. Comparing Figure 8a with Figure 8b demonstrates that, while the dynamical behaviors of the two lasers are symmetric over most of the operating conditions considered here, asymmetry breaking happens mainly over a region where  $\zeta_{12}^e$  falls between 0.17 and 0.24 and  $f_i$  is around 10 GHz and mildly over a region where  $\zeta_{12}^e$  is around 0.16 and  $f_i$  is around  $-20 \text{ GHz}$ . Compared with Figure 3(a-ii) and Figure 3(b-ii), the experimental observations on the distribution of different dynamical states greatly agree with the numerical predictions, except for the P2 dynamical states appearing on the right-upper corner of Figure 3.

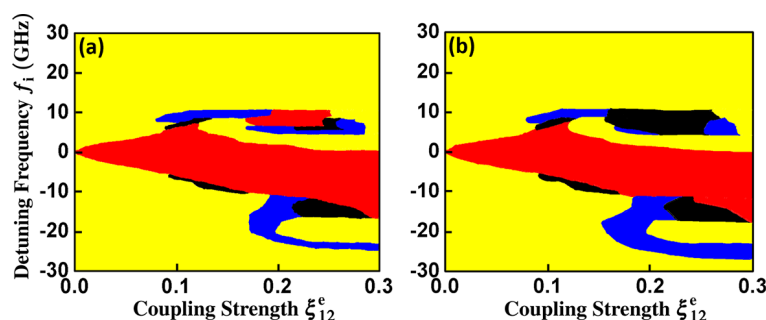


**Figure 8.** Maps of dynamical states for (a) LD1 and (b) LD2, respectively, in the mutually coupled laser system when  $\zeta_{21}^e = 0.01$ . Regions of mutual injection locking, P1 dynamics, P2 dynamics, and chaos are marked by red, yellow, blue, and black, respectively.

To study how the dynamical behaviors of both lasers develop from symmetry to asymmetry when  $\zeta_{21}^e = 0.01$ , a progression of optical and microwave spectra for LD1 (red curve) and LD2 (black curve) is presented in Figure 9a and Figure 9b, respectively, when  $\zeta_{12}^e$  is adjusted and  $f_i$  is fixed at 10 GHz. At  $\zeta_{12}^e = 0.019$ , either LD1 or LD2 behaves as a P1 dynamical state with an oscillation frequency of about 10 GHz, as either Figure 9(a-i) or

Figure 9(b-i) demonstrates. As  $\zeta_{12}^e$  is increased to 0.064, either LD1 or LD2 still behaves as a P1 dynamical state yet with an oscillation frequency of about 9.4 GHz, as either Figure 9(a-ii) or Figure 9(b-ii) presents. While the microwave spectral features of both lasers look highly similar in Figure 9(b-ii), a slight deviation exists in their optical spectral features in Figure 9(a-ii). Not only do a few more spectral components emerge in LD2, but the principal oscillation also becomes less dominant, making the optical spectral profile of LD2 more widely distributed. This implies that the two lasers start to behave differently in a subtle manner even though they both behave as a P1 dynamical state. Such a deviation becomes more significant when  $\zeta_{12}^e$  is further increased to 0.151, as Figure 9(a-iii) shows. Both lasers now evolve into a P2 dynamical state, as more evidently observed in Figure 9(b-iii), where subharmonics emerge in the midway of spectral components at the integral multiples of 11.9 GHz.

As  $\zeta_{12}^e$  is continued to increase to 0.213, both optical and microwave spectra of the two lasers shown in Figure 9(a-iv,b-iv) exhibit completely different spectral features. On one hand, as Figure 9(a-iv) presents, LD1 oscillates at an offset frequency of 9.47 GHz that is surrounded by two low-intensity spectral components about 11.7 GHz away. The two low-intensity components result from the modified relaxation resonance of LD1 due to the optical injection from LD2, which is more clearly identified in Figure 9(b-iv) where a small bump appears at around 11.7 GHz. This indicates that LD1 now emits a continuous-wave optical output with a slightly higher relaxation resonance frequency as compared with its free-running condition. On the other hand, as either Figure 9(a-iv) or Figure 9(b-iv) shows, a broad and continuous spectral distribution is observed for LD2, indicating that LD2 now behaves as a chaotic state. By further increasing  $\zeta_{12}^e$  to 0.3, either LD1 or LD2 behaves as a P1 dynamical state with an oscillation frequency of about 16 GHz, as either Figure 9(a-v) or Figure 9(b-v) demonstrates. While the microwave spectral features of both lasers look similar in Figure 9(b-v), a slight deviation exists in their optical spectral features in Figure 9(a-v). Not only do a few more spectral components emerge in LD2, but the principal oscillation also becomes less dominant, making the optical spectral profile of LD2 more widely distributed. This implies that the two lasers behave differently in a subtle manner even though they both behave as a P1 dynamical state. Comparing Figure 9 with Figure 4 demonstrates that the experimental observations on the evolution of the dynamical behaviors from symmetry to asymmetry agree well with the numerical predictions.

The extremest case for the dynamical behavior asymmetry happens when no optical injection is introduced from LD2 to LD1, i.e.,  $\zeta_{21}^e = 0$ . Under such an operating condition, the distribution of dynamical states as a function of  $\zeta_{12}^e$  and  $f_1$  for LD2 is greatly similar to the one presented in Figure 8b, while LD1 is kept at its free-running operation and thus emits a continuous-wave optical output no matter how  $\zeta_{12}^e$  and  $f_1$  are adjusted.

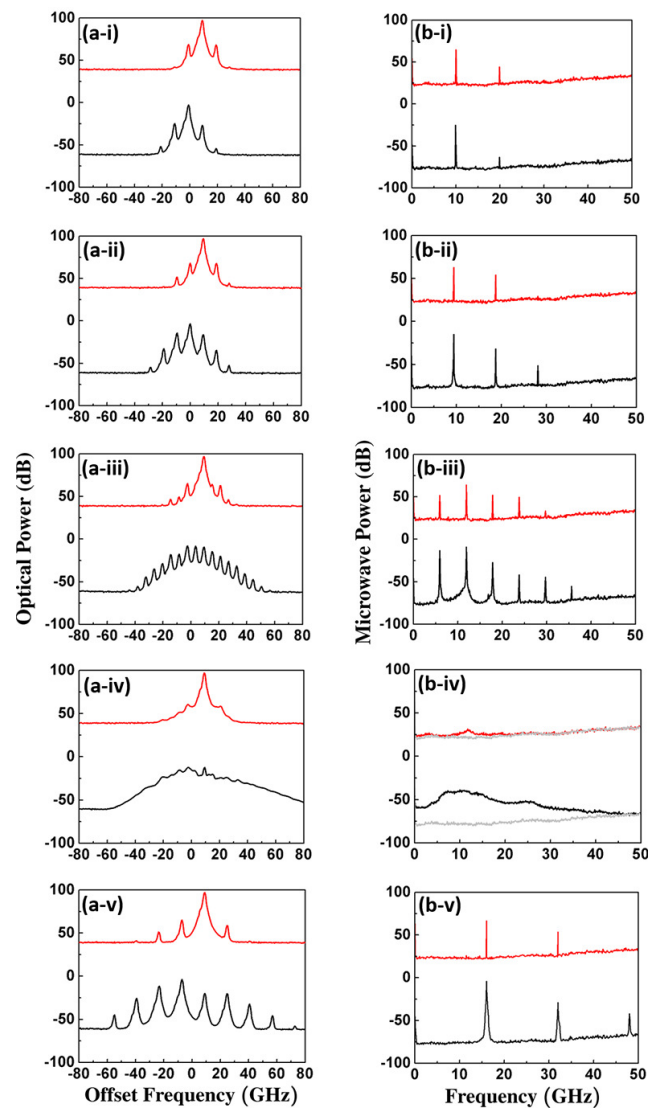


**Figure 9.** (a) Optical spectra and (b) microwave spectra of LD1 (red curve) and LD2 (black curve) for (i)  $\zeta_{12}^e = 0.019$ , (ii)  $\zeta_{12}^e = 0.064$ , (iii)  $\zeta_{12}^e = 0.151$ , (iv)  $\zeta_{12}^e = 0.213$ , and (v)  $\zeta_{12}^e = 0.3$ , respectively, when  $\zeta_{21}^e = 0.01$  and  $f_i = 10$  GHz. The  $x$ -axes in (a) are relative to the free-running oscillation frequency of LD2. The red curves in (a,b) are up-shifted by 100 dB for clear visibility. The gray curves in (b-iv) show the noise floor of the laser system.

#### 4. Conclusions

This study experimentally and numerically investigates the effects of asymmetric coupling strength on nonlinear dynamics of two mutually coupled semiconductor lasers with a delay time longer than the relaxation resonance period of either laser at free running. Symmetry in the coupling strength of the two lasers, in general, symmetrizes their dynamical behaviors and the corresponding spectral features. Slight to moderate asymmetry in the coupling strength moderately changes their dynamical behaviors from the ones when the coupling strength is symmetric, but does not break the symmetry of their dynamical behaviors and the corresponding spectral features. The former suggests that if a specific dynamical behavior is used for applications where a difference in the coupling strength between the two lasers is likely to happen in order to achieve certain features or functionalities, care must be taken so that the laser system is operated at the same dynamical behavior even when the coupling strength becomes asymmetric during operation. High asymmetry in the coupling strength not only strongly changes their dynamical behaviors from the ones when the coupling strength is symmetric, but also breaks the symmetry of their dynamical

behaviors and the corresponding spectral features. This suggests that if both lasers are expected to simultaneously operate at a specific dynamical behavior all the time for applications, care must be taken either to avoid the operation of the laser system with highly asymmetric coupling strength, or to avoid the operation of the laser system over regions where symmetry breaking in the dynamical behavior happens. Evolution of the dynamical behaviors from symmetry to asymmetry between the two lasers is observed. The numerical model used here reproduces the experimental observations not only qualitatively to a high extent but also quantitatively to a moderate extent.

**Author Contributions:** Conceptualization, S.-K.H.; experiment, C.-H.T. and Y.-C.C.; simulation, B.-K.L. and C.-H.T.; writing, C.-H.T. and S.-K.H. All authors have read and agreed to the published version of the manuscript.

**Funding:** This research was funded by the Ministry of Science and Technology, Taiwan under contract MOST-106-2112-M-006-004-MY3 and MOST-109-2112-M-006-018-MY3.

**Data Availability Statement:** Data underlying the results presented in this paper are not publicly available at this time but may be obtained from the authors upon reasonable request.

**Conflicts of Interest:** The authors declare no conflict of interest.

## References

1. Chrostowski, L.; Shi, W. Monolithic injection-locked high-speed semiconductor ring lasers. *J. Light. Technol.* **2008**, *26*, 3355–3362. [[CrossRef](#)]
2. Chow, W.W.; Yang, Z.S.; Vawter, G.A.; Skogen, E.J. Modulation response improvement with isolator-free injection-locking. *IEEE Photonics Technol. Lett.* **2009**, *21*, 839–841. [[CrossRef](#)]
3. Tauke-Pedretti, A.; Vawter, G.A.; Skogen, E.J.; Peake, G.; Overberg, M.; Alford, C.; Chow, W.W.; Yang, Z.S.; Torres, D.; Cajas, F. Mutual injection locking of monolithically integrated coupled-cavity DBR lasers. *IEEE Photonics Technol. Lett.* **2011**, *23*, 908–910. [[CrossRef](#)]
4. Yang, Z.; Tauke-Pedretti, A.; Vawter, G.A.; Chow, W.W. Mechanism for modulation response improvement in mutually injection-locked semiconductor lasers. *IEEE J. Quantum Electron.* **2011**, *47*, 300–305. [[CrossRef](#)]
5. Xiao, Z.X.; Huang, Y.Z.; Yang, Y.D.; Tang, M.; Xiao, J.L. Modulation bandwidth enhancement for coupled twin-square microcavity lasers. *Opt. Lett.* **2017**, *42*, 3173–3176. [[CrossRef](#)] [[PubMed](#)]
6. Sun, C.; Liu, D.; Xiong, B.; Luo, Y.; Wang, J.; Hao, Z.; Han, Y.; Wang, L.; Li, H. Modulation characteristics enhancement of monolithically integrated laser diodes under mutual injection locking. *IEEE J. Sel. Top. Quantum Electron.* **2015**, *21*, 628–635. [[CrossRef](#)]
7. Zhang, Y.; Li, L.; Zhou, Y.; Zhao, G.; Shi, Y.; Zheng, J.; Zhang, Z.; Liu, Y.; Zou, L.; Zhou, Y.; et al. Modulation properties enhancement in a monolithic integrated two-section DFB laser utilizing side-mode injection locking method. *Opt. Express* **2017**, *25*, 27595–27608. [[CrossRef](#)]
8. Zheng, J.; Zhao, G.; Zhou, Y.; Zhang, Z.; Pu, T.; Shi, Y.; Zhang, Y.; Liu, Y.; Li, L.; Lu, J.; et al. Experimental demonstration of amplified feedback DFB Laser with modulation bandwidth enhancement based on the reconstruction equivalent chirp technique. *IEEE Photonics J.* **2017**, *9*, 1–8. [[CrossRef](#)]
9. Chien, C.-Y.; Lo, Y.-H.; Wu, Y.-C.; Hsu, S.-C.; Tseng, H.-R.; Lin, C.-C. Compact photonic integrated chip for tunable microwave generation. *IEEE Photonics Technol. Lett.* **2014**, *26*, 490–493. [[CrossRef](#)]
10. Lo, Y.H.; Wu, Y.C.; Hsu, S.C.; Hwang, Y.C.; Chen, B.C.; Lin, C.C. Tunable microwave generation of a monolithic dual-wavelength distributed feedback laser. *Opt. Express* **2014**, *22*, 13125–13137. [[CrossRef](#)]
11. Zhang, X.; Zheng, J.; Pu, T.; Zhang, Y.; Shi, Y.; Li, J.; Li, Y.; Zhu, H.; Chen, X. Simple frequency-tunable optoelectronic oscillator using integrated multi-section distributed feedback semiconductor laser. *Opt. Express* **2019**, *27*, 7036–7046. [[CrossRef](#)]
12. Zhou, Y.; Lu, Z.; Li, L.; Zhang, Y.; Zheng, J.; Du, Y.; Zou, L.; Shi, Y.; Zhang, X.; Chen, Y.; et al. Tunable microwave generation utilizing monolithic integrated two-section DFB laser. *Laser Phys.* **2019**, *29*, 046201. [[CrossRef](#)]
13. Fujino, H.; Ohtsubo, J. Synchronization of chaotic oscillations in mutually coupled semiconductor lasers. *Opt. Rev.* **2001**, *8*, 351–357. [[CrossRef](#)]
14. Gross, N.; Kinzel, W.; Kanter, I.; Rosenbluh, M.; Khaykovich, L. Synchronization of mutually versus unidirectionally coupled chaotic semiconductor lasers. *Opt. Commun.* **2006**, *267*, 464–468. [[CrossRef](#)]
15. Mengue, A.D.; Essimbi, B.Z. Secure communication using chaotic synchronization in mutually coupled semiconductor lasers. *Nonlinear Dyn.* **2012**, *70*, 1241–1253. [[CrossRef](#)]
16. Yan, S.L. Chaotic synchronization of two mutually coupled semiconductor lasers for optoelectronic logic gates. *Commun. Nonlinear Sci. Numer. Simul.* **2012**, *17*, 2896–2904.
17. Hou, Y.S.; Xia, G.Q.; Jayaprasath, E.; Yue, D.Z.; Yang, W.Y.; Wu, Z.M. Prediction and classification performance of reservoir computing system using mutually delay-coupled semiconductor lasers. *Opt. Commun.* **2019**, *433*, 215–220. [[CrossRef](#)]

18. Hou, Y.S.; Xia, G.Q.; Jayaprasath, E.; Yue, D.Z.; Wu, Z.M. Parallel information processing using a reservoir computing system based on mutually coupled semiconductor lasers. *Appl. Phys. B-Lasers Opt.* **2020**, *126*, 40. [[CrossRef](#)]
19. Liang, W.Y.; Xu, S.R.; Jiang, L.; Jia, X.H.; Lin, J.B.; Yang, Y.L.; Liu, L.M.; Zhang, X. Design of parallel reservoir computing by mutually-coupled semiconductor lasers with optoelectronic feedback. *Opt. Commun.* **2021**, *495*, 127120. [[CrossRef](#)]
20. Mihana, T.; Mitsui, Y.; Takabayashi, M.; Kanno, K.; Sunada, S.; Naruse, M.; Uchida, A. Decision making for the multi-armed bandit problem using lag synchronization of chaos in mutually coupled semiconductor lasers. *Opt. Express* **2019**, *27*, 26989–27008. [[CrossRef](#)]
21. Heil, T.; Fischer, I.; Elsasser, W.; Mulet, J.; Mirasso, C.R. Chaos synchronization and spontaneous symmetry-breaking in symmetrically delay-coupled semiconductor lasers. *Phys. Rev. Lett.* **2001**, *86*, 795–798. [[CrossRef](#)]
22. Rogister, F.; Garcia-Ojalvo, J. Symmetry breaking and high-frequency periodic oscillations in mutually coupled laser diodes. *Opt. Lett.* **2003**, *28*, 1176–1178. [[CrossRef](#)]
23. Mulet, J.; Mirasso, C.; Heil, T.; Fischer, I. Synchronization scenario of two distant mutually coupled semiconductor lasers. *J. Opt. B Quantum Semiclass. Opt.* **2004**, *6*, 97–105. [[CrossRef](#)]
24. Junges, L.; Gavrielides, A.; Gallas, J.A.C. Synchronization properties of two mutually delay-coupled semiconductor lasers. *J. Opt. Soc. Am. B-Opt. Phys.* **2016**, *33*, C65–C71. [[CrossRef](#)]
25. Seifika, M.; Amann, A.; Peters, F.H. Dynamics of two identical mutually delay-coupled semiconductor lasers in photonic integrated circuits. *Appl. Opt.* **2018**, *57*, E37–E44. [[CrossRef](#)] [[PubMed](#)]
26. Lingnau, B.; Perrott, A.H.; Dernaika, M.; Caro, L.; Peters, F.H.; Kelleher, B. Dynamics of on-chip asymmetrically coupled semiconductor lasers. *Opt. Lett.* **2020**, *45*, 2223–2226. [[CrossRef](#)] [[PubMed](#)]
27. Simpson, T.B.; Liu, J.M. Phase and amplitude characteristics of nearly degenerate four-wave mixing in Fabry-Perot semiconductor lasers. *J. Appl. Phys.* **1993**, *73*, 2587–2589. [[CrossRef](#)]
28. Liu, J.M.; Simpson, T.B. Four-wave mixing and optical modulation in a semiconductor laser. *IEEE J. Quantum Electron.* **1994**, *30*, 957–965.
29. Simpson, T.B.; Liu, J.M.; Huang, K.F.; Tai, K. Nonlinear dynamics induced by external optical injection in semiconductor lasers. *Quantum Semiclass. Opt.* **1997**, *9*, 765–784. [[CrossRef](#)]
30. Hwang, S.K.; Liu, J.M. Dynamical characteristics of an optically injected semiconductor laser. *Optics Communications. Opt. Commun.* **2000**, *183*, 195–205. [[CrossRef](#)]
31. Simpson, T.B.; Liu, J.M. Spontaneous emission, nonlinear optical coupling, and noise in laser diodes. *Opt. Commun.* **1994**, *112*, 43–47. [[CrossRef](#)]
32. Hwang, S.K.; Liu, J.M.; White, J.K. 35-GHz intrinsic bandwidth for direct modulation in 1.3- $\mu\text{m}$  semiconductor lasers subject to strong injection locking. *IEEE Photonics Technol. Lett.* **2004**, *16*, 972–974. [[CrossRef](#)]
33. Chan, S.C. Analysis of an optically injected semiconductor laser for microwave generation. *IEEE J. Quantum Electron.* **2010**, *46*, 421–428. [[CrossRef](#)]
34. Simpson, T.B.; Liu, J.M.; AlMulla, M.; Usechak, N.G.; Kovanis, V. Linewidth sharpening via polarization-rotated feedback in optically injected semiconductor laser oscillators. *IEEE J. Sel. Top. Quantum Electron.* **2013**, *19*, 1500807. [[CrossRef](#)]
35. Lo, K.H.; Hwang, S.K.; Donati, S. Optical feedback stabilization of photonic microwave generation using period-one nonlinear dynamics of semiconductor lasers. *Opt. Express* **2014**, *22*, 18648–18661. [[CrossRef](#)]
36. Lo, K.H.; Hwang, S.K.; Donati, S. Numerical study of ultrashort-optical-feedback-enhanced photonic microwave generation using optically injected semiconductor lasers at period-one nonlinear dynamics. *Opt. Express* **2017**, *25*, 31595–31611. [[CrossRef](#)]
37. Zhang, L.; Chan, S.C. Cascaded injection of semiconductor lasers in period-one oscillations for millimeter-wave generation. *Opt. Lett.* **2019**, *44*, 4905–4908. [[CrossRef](#)]
38. Tseng, C.H.; Lin, C.T.; Hwang, S.K. V- and W-band microwave generation and modulation using semiconductor lasers at period-one nonlinear dynamics. *Opt. Lett.* **2020**, *45*, 6819–6822. [[CrossRef](#)]
39. Lin, F.Y.; Liu, J.M. Chaotic radar using nonlinear laser dynamics. *IEEE J. Quantum Electron.* **2004**, *40*, 815–820. [[CrossRef](#)]
40. Xu, H.; Wang, B.J.; Han, H.; Liu, L.; Li, J.X.; Wang, Y.C.; Wang, A.B. Remote imaging radar with ultra-wideband chaotic signals over fiber links. *Int. J. Bifurc. Chaos* **2015**, *25*, 1530029. [[CrossRef](#)]
41. Wang, L.S.; Guo, Y.Y.; Li, P.; Zhao, T.; Wang, Y.C.; Wang, A.B. White-chaos radar with enhanced range resolution and anti-jamming capability. *IEEE Photon. Technol. Lett.* **2017**, *29*, 1723–1726. [[CrossRef](#)]
42. Tseng, C.H.; Hwang, S.K. Broadband chaotic microwave generation through destabilization of period-one nonlinear dynamics in semiconductor lasers for radar applications. *Opt. Lett.* **2020**, *45*, 3777–3780. [[CrossRef](#)]
43. Pecora, L.M.; Carroll, T.L.; Johnson, G.A.; Mar, D.J.; Heagy, J.F. Fundamentals of synchronization in chaotic systems, concepts, and applications. *Chaos* **1997**, *7*, 520–543. [[CrossRef](#)] [[PubMed](#)]
44. VanWiggeren, G.D.; Roy, R. Communication with chaotic lasers. *Science* **1998**, *279*, 1198–1200. [[CrossRef](#)]
45. Argyris, A.; Syvridis, D.; Larger, L.; Annovazzi-Lodi, V.; Colet, P.; Fischer, I.; Garcia-Ojalvo, J.; Mirasso, C.R.; Pesquera, L.; Shore, K.A. Chaos-based communications at high bit rates using commercial fibre-optic links. *Nature* **2005**, *438*, 343–346. [[CrossRef](#)]
46. Uchida, A.; Rogister, F.; Garcia-Ojalvo, J.; Roy, R. Synchronization and communication with chaotic laser systems. *Prog. Opt.* **2005**, *48*, 203–341.

47. Uchida, A.; Amano, K.; Inoue, M.; Hirano, K.; Naito, S.; Someya, H.; Oowada, I.; Kurashige, T.; Shiki, M.; Yoshimori, S.; et al. Fast physical random bit generation with chaotic semiconductor lasers. *Nat. Photonics* **2008**, *2*, 728–732. [[CrossRef](#)]
48. Hart, J.D.; Terashima, Y.; Uchida, A.; Baumgartner, G.B.; Murphy, T.E.; Roy, R. Recommendations and illustrations for the evaluation of photonic random number generators. *APL Photonics* **2017**, *2*, 090901-1–090901-22. [[CrossRef](#)]
49. Wang, A.; Wang, L.; Li, P.; Wang, Y. Minimal-post-processing 320-Gbps true random bit generation using physical white chaos. *Opt. Express* **2017**, *25*, 3153–3164. [[CrossRef](#)]
50. Tseng, C.H.; Funabashi, R.; Kanno, K.; Uchida, A.; Wei, C.C.; Hwang, S.K. High-entropy chaos generation using semiconductor lasers subject to intensity-modulated optical injection for certified physical random number generation. *Opt. Lett.* **2021**, *46*, 3384–3387. [[CrossRef](#)] [[PubMed](#)]